Quantification and Description of Distance Measurement Errors of a Time-of-Flight Camera

Tim Pattinson

Institute for Photogrammetry, Stuttgart University, Germany

Abstract. This study assesses the accuracy of distance measurements made by a time-of-flight camera, the PMD CamCube 2.0. The camera is calibrated using a planar test field, and various models are proposed for the systematic errors.

Compared to models using polynomial functions of distance, a sinusoidal model is found to perform well using wavelengths of one quarter or one eighth of the modulation wavelength. These are then combined with a radial term, giving the final 7-parameter model. When applied to the data, rms errors between 10.5 and 11.1 mm are obtained, and with an independent measurement set, between 11.4 and 12.4 mm.

On examination of the theory, the eighth-wavelength terms appear to originate from an impure modulation signal with third and fifth harmonics. The sensitivity to temperature is also shown to be consistent with changes in the modulation frequency.

1 Introduction

In order to calibrate the camera's distance measurements, it is necessary to compare sets of these measurements with known distances. For this, a (nominally) planar test field was used, with a 7-by-7 grid of large, circular targets. This test field was already constructed on the wall of a basement test room, and was specially designed for the lower spatial resolution of this PMD camera. The white circles on the targets were selected so that they would be represented by several pixels on these camera's images, with small black dots at each centre to allow precise positioning by higher-resolution equipment.

Figure 1 shows the camera mounted on a tripod facing the test field. Each of the 49 white circles in the field presents a large, highly-reflective target for the camera. Note that due to the design of the test field, the distance measurements are all made within a uniform, reflective surface. This avoids some of the edge effects encountered with checkerboard patterns, where the distance measurements are taken at the boundary between dark and light sections.

By taking the known target coordinates and a set of intensity images from the PMD camera, the position of the camera for each image can then be determined, and therefore the geometrical distances to each of the targets. By comparing these geometrical distances with the measured distances from the camera's range image, the errors can be determined and evaluated.

1.1   Measurements

The test field is shown in figure 1. In order to cover a large range of distances, several camera stations were used as shown in figure 2. This "chain" was constructed off-axis so that each image has a greater range of distances, and so that coverage overlaps between images. In this chain, all four camera orientations were also used equally to avoid bias.
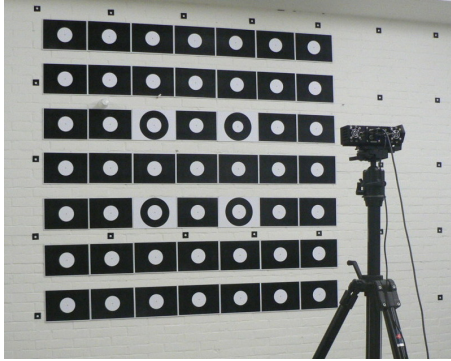
Fig. 1: Camera facing the test field
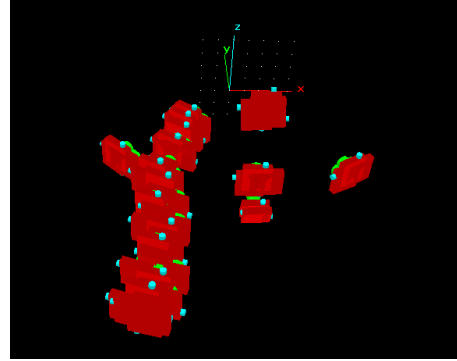
Fig. 2: Calculated camera positions

Figure 3 shows the measurement errors as a function of geometrical distance. A wave-like pattern is clearly visible.
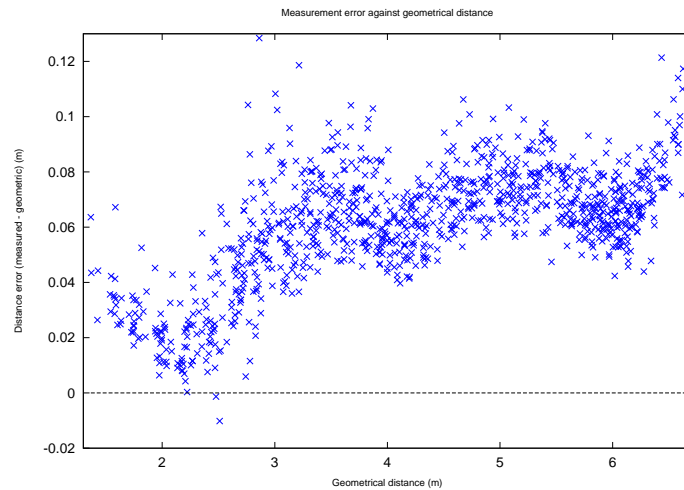
Fig. 3: Plot of measurement errors against geometrically calculated distances

Several interesting features emerge from this figure:

– Almost all the errors are greater than zero, which means that the distance
  measurements from the camera are generally slightly higher than the geo-
  metrically calculated distances.
– The maximum error is on the order of 12 cm, with most of them below 8 cm.
– Errors are generally larger for larger distances.
– There is a marked wave-like structure in the error data, which does not
  appear to be random.
– The errors are clustered fairly well in the vertical direction, which implies a
  large systematic component. Therefore, calibration should be successful in
  reducing the size of the errors.

1.2   Temperature Dependence

As previously noted by other authors [1], it was found that after prolonged use
of the camera, the camera became warm and the measured distances increased
noticeably. To examine this in more detail, repeated exposures were taken of
a corridor wall, and repeated after 10 minutes of continuous use at high frame
rate. Figure 4 shows a comparison of the measurements for all four frequencies,
plotting the ratio of warm distance to cool distance.

Although there is a great deal of noise present, especially at longer distances,
the ratio is always greater than 1, meaning that the distances measured after
warming are always greater. Furthermore, the ratio is remarkably constant, be-
tween 1.01 and 1.02, with the majority at around 1.015. This implies a reasonably
constant increase in distance of between 1% and 2%, which is consistent with an
increase of modulation frequency of the same magnitude.
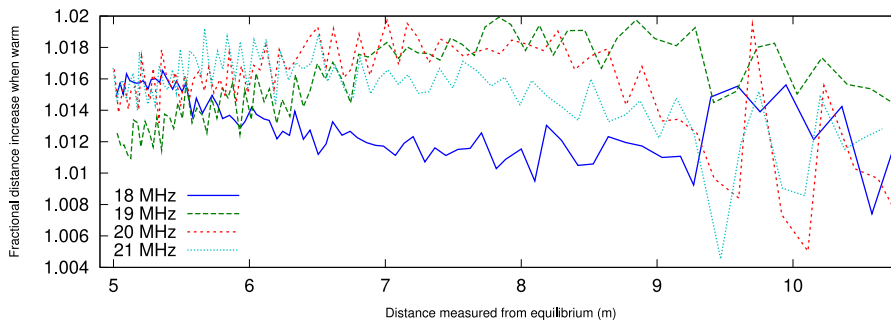
Fig. 4: Ratio of measured distances after camera warming

Also, the wraparound point, at which the measured distance reaches its max-
imum and drops to near zero, occurred closer to the camera after warming, which
is also consistent with an increase of modulation frequency.

2   Calibration Models

The data shown in figure 3 was analysed using Gnu Octave to fit models of varying complexity. An ideal model would match the data accurately leaving a small residual error, while requiring a small number of arbitrary parameters. Each model was applied to data from each of the four available modulation frequencies used by this camera (18 MHz, 19 MHz, 20 MHz and 21 MHz).

2.1   Polynomial Models

With the raw data, the rms error is 6.5 cm on distance measurements between 1.5 and 7 metres. The simplest correction possible is to subtract a fixed offset from each measurement, in this case 6.1 cm, which brings down the rms error to just 2.0 cm. A linear fit with two parameters is more successful, reducing the rms error to 1.6 cm.

This can be extended to polynomials of arbitrary complexity, with the best results coming from a 5-parameter polynomial (rms 1.38 cm) and a 7-parameter polynomial (rms 1.27 cm). However these models give no insight into the meaning of the coefficients or the cause of the errors.

2.2   Sinusoidal Model

Because of the obvious wave-like distribution of the errors in figure 3, one possible choice of model is a sinusoidal wave of unknown wavelength. This would lead to a more satisfactory description of the trend than a set of polynomial coefficients. A single wave with amplitude, wavelength and phase was therefore added to the linear fit (comprising offset and scale) to give a 5-parameter model which yielded an rms error of 1.40 cm. This is a similar result to the 5-parameter polynomial but the parameters are more meaningful.

In this case, especially the fitted wavelength is of interest because for the 20 MHz and 21 MHz data, it was found to correspond closely to one eighth of the corresponding modulation wavelength. For the 18 MHz and 19 MHz data, the fit was close to one quarter of the modulation wavelength. These surprising results led to an extension of the model to include both sinusoidal waves using 6 parameters.

2.3   Double Sinusoidal Model

Using two sinusoidal waves instead of one, the model equation becomes:

$$\Delta d = a_0 + a_1 d + a_2 \cos(4kd) + a_3 \sin(4kd) + a_4 \cos(8kd) + a_5 \sin(8kd) \qquad (1)$$

where k is the wavenumber related to the camera's modulation frequency f_{mod} :

$$k = \frac{2\pi}{\lambda_{mod}} = \frac{2\pi f_{mod}}{c} \qquad (2)$$

Here, a_0 is the offset, a_1 the scale correction, a_2 and a_3 correspond to the quarter-wavelength waves, and a_4 and a_5 are the amplitudes of the eighth-wavelength waves.

The six parameter values are found using a single least-squares adjustment. It can be seen graphically in figure 5 that this model is successful at matching the data despite its small number of parameters. Subtraction of the model from each data set gives a lower point cloud, much closer to the zero axis.

After applying this model to the measurements, the rms errors range from a mere 1.22 cm (for 21 MHz) up to 1.29 cm (for 18 MHz).

(a) Fit for 18 MHz

(b) Fit for 19 MHz

(c) Fit for 20 MHz

(d) Fit for 21 MHz
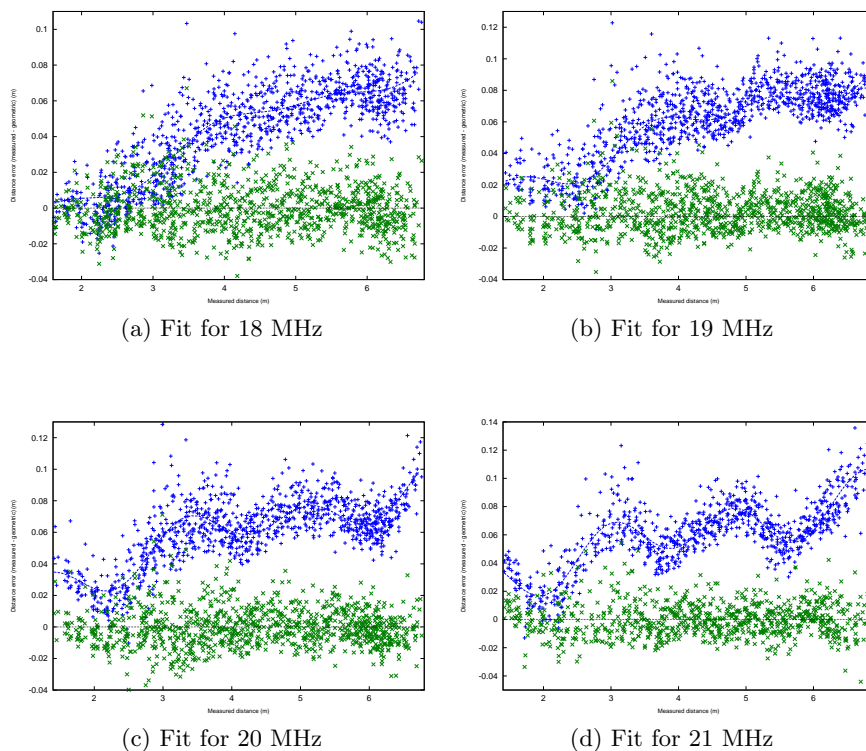
Fig. 5: Double sinusoidal fits for all four modulation frequencies

2.4 Radial Anomalies

On closer examination of the remaining residuals, they were found to conform to a consistent pattern according to their position on the image plane. As shown in figure 6, the measurements which are too high are clustered around the corners of the images, and those in the centre of the image are mostly slightly too low.

Image plane

■ Measurement too long after correction
■ Measurement too short after correction
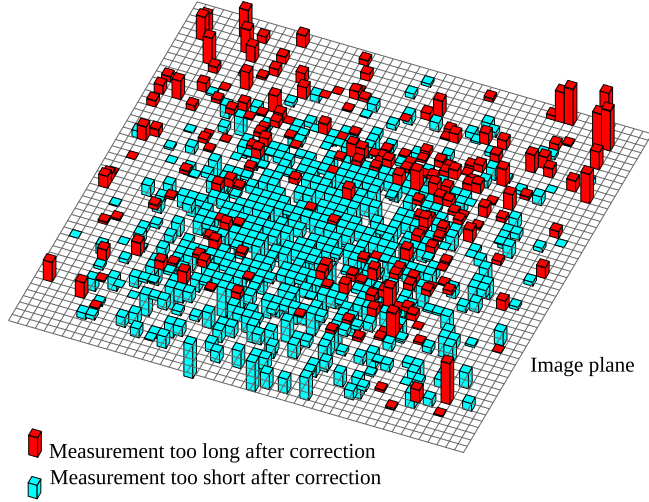
Fig. 6: Error distribution over image plane

This effect can be modelled most simply by a linear term in radial distance, requiring a seventh calibration parameter.

2.5   Final Model

After adding the radial term to equation 1, we obtain the following final seven-parameter model for the calibration, using the measured distance d and the radial distance in the image plane r:

$$\Delta d = a_0 + a_1 d + a_2 \cos(4kd) + a_3 \sin(4kd) + a_4 \cos(8kd) + a_5 \sin(8kd) + a_6 r \quad (3)$$

To apply this calibration to measurements taken from the camera, the calculated error Δd needs to be subtracted from each of the measurements, to give the corrected distance d_{corr}:

$$d_{corr} = d - \Delta d \quad (4)$$

3   Theory

Now that a successful model has been derived which matches the systematic errors, the next step is to inspect the terms in the model to find possible origins. Apart from the simple offset and scale parameters a_0 and a_1, the most interesting terms are the sinusoidal waves with wavelengths one quarter or one eighth of the modulation wavelength.

3.1   Phase Measurements

Firstly, we treat the modulation signal as an ideal sine wave, and examine the calculations made. The PMD sensor samples the reflected signal at four narrow, equally-spaced intervals, synchronised with the output signal. Using these values it is able to reconstruct the amplitude and phase of the reflection and hence the distance to the object. For a relative phase shift of ψ, the samples should be:

$$
\begin{aligned}
s_1 &= m \sin \psi + b \\
s_2 &= m \sin(\psi + \tfrac{\pi}{2}) + b = m \cos \psi + b \\
s_3 &= m \sin(\psi + \pi) + b = -m \sin \psi + b \\
s_4 &= m \sin(\psi + \tfrac{3\pi}{2}) + b = -m \cos \psi + b
\end{aligned}
\tag{5}
$$

And by subtracting these terms and dividing, the calculated phase ϕ is equal to the actual phase:

$$
\phi = \tan^{-1}\left(\frac{s_1 - s_3}{s_2 - s_4}\right) = \psi
\tag{6}
$$

Therefore, if the output signal is a pure sine wave, the phase determination will be accurate. The distance d is calculated using the modulation wavelength λ_{mod}:

$$
d = \frac{\phi}{2\pi} \frac{\lambda_{mod}}{2}
\tag{7}
$$

3.2   Eighth-Wavelength Terms

As previously discussed by Rapp [4], it can be supposed that due to the difficulties of generating a completely pure sinusoidal signal, a small component of the third harmonic is included as well. If we denote the (small) relative amplitude of this component by ϵ, then the equations are modified:

$$
\begin{aligned}
s_1 &= m \sin \psi + m\epsilon \sin(3\psi) + b \\
s_2 &= m \sin(\psi + \tfrac{\pi}{2}) + m\epsilon \sin(3\psi + \tfrac{3\pi}{2}) + b = m \cos \psi - m\epsilon \cos(3\psi) + b \\
s_3 &= m \sin(\psi + \pi) + m\epsilon \sin(3\psi + 3\pi) + b = -m \sin \psi - m\epsilon \sin(3\psi) + b \\
s_4 &= m \sin(\psi + \tfrac{3\pi}{2}) + m\epsilon \sin(3\psi + \tfrac{9\pi}{2}) + b = -m \cos \psi + m\epsilon \cos(3\psi) + b
\end{aligned}
\tag{8}
$$

Then the calculated phase ϕ is no longer equal to the actual phase ψ:

$$
\phi = \tan^{-1}\left(\frac{\sin \psi + \epsilon \sin(3\psi)}{\cos \psi - \epsilon \cos(3\psi)}\right)
\tag{9}
$$

It can be shown by differentiation that for small ϵ, the effect of this third harmonic on the calculated phase ϕ is also sinusoidal with frequency 4ψ:

$$
\phi = \psi + \epsilon \sin(4\psi)
\tag{10}
$$

This can be visualised by taking a unit vector at angle ψ, and adding a smaller vector of length ϵ subtending an angle 3ψ. This is outlined in figure 7.

As the unit vector rotates, and the smaller vector rotates at three times the speed in the opposite direction, the angle subtended by the tip of the smaller vector at the origin follows ψ roughly but with a disturbance according to the size of ϵ. This disturbance is governed by the relative orientation of the two vectors, which undergoes four cycles due to the opposite rotation directions.
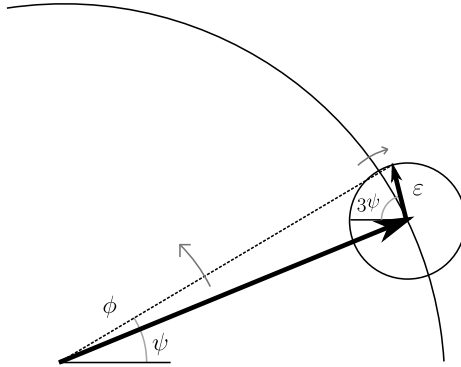
Fig. 7: Effect of the third harmonic due to counter-rotating vectors

Thus it can be seen that if the outgoing modulation signal contains a small component of the third harmonic, the end result will be a sinusoidal disturbance of the phase measurements. These will undergo four cycles in the range from 0 to 2π, which results in a sinusoidal modulation of the distance measurements with wavelength one eighth of the modulation wavelength, as observed.

This examination can be repeated supposing a component of the fifth harmonic, and this produces a very similar result. For small ϵ, the effect on the distance measurements is the same, also causing a modulation with wavelength one eighth of the modulation wavelength.

The amplitudes of the eighth-wavelength fluctuations were calculated to be between 0.35 cm (for 18 MHz) and 1.49 cm (for 21 MHz). This means that for the 18 MHz signal, ϵ is less than 0.3%, but this rises to 0.9% for 20 MHz and 1.3% for the maximum 21 MHz. These values indicate that the signal is basically sinusoidal, with 3rd and/or 5th harmonics on the order of 1%.

3.3   Quarter-Wavelength Terms

The origin of the quarter-wavelength terms in the model are still unexplained. If we picture the PMD sensor containing two active sensor elements, as described for example by Ringbeck [5], we might imagine that the areas of the two sensor parts might not be exactly identical. Perhaps there is a slight difference in the collecting area, or the amplification, inherent to the design. We can follow the

consequence by supposing a constant scale factor γ which is close to, but not exactly equal to 1.

Then if we re-examine the equations, and apply the constant factor γ to the sample values s_1 and s_3, we again get a slight disturbance to the phase measurements and a resulting disturbance to the distance calculations:

$$
\begin{aligned}
s_1 &= m\gamma \sin\psi + b \\
s_2 &= m\sin(\psi + \tfrac{\pi}{2}) + b = m\cos\psi + b \\
s_3 &= m\gamma\sin(\psi + \pi) + b = -m\gamma\sin\psi + b \\
s_4 &= m\sin(\psi + \tfrac{3\pi}{2}) + b = -m\cos\psi + b
\end{aligned}
\tag{11}
$$

And the calculated phase is again shifted from the true phase:

$$
\tan\phi = \gamma\tan\psi \tag{12}
$$

Again by differentiation, it can be shown that this leads to a sinusoidal variation of the phase with frequency 2ψ, and therefore a sinusoidal variation of the calculated distance with wavelength of a quarter of the modulation wavelength. So if there were such an asymmetry, such an effect would account for the quarter-wavelength terms found earlier.

The adjustment gave amplitudes of the quarter-wavelength signal between 0.80 cm and 0.94 cm, which corresponds to phase discrepancies between 0.0063 and 0.0079 radians. This would be caused by a scale factor γ of between 1.012 and 1.016, meaning an asymmetry of around 1% between the two halves of the PMD sensor. However, to explain the observed fluctuations it would have to be an asymmetry affecting all the pixels in the sensor, whether related to size, amplification or timing of the sensor components.

4   Conclusion

A variety of models were presented to explain the systematic distance measurement errors using polynomials and sinusoidal functions. The best results were obtained by a combined model using 7 calibration parameters. These parameters were calculated for all four of the camera's modulation frequency settings, from 18 MHz to 21 MHz, using equation 3.

In addition, the physical significance of these calibration parameters was investigated, to identify the effects behind them. This transforms the calibration exercise from purely numerical data manipulation into a meaningful description of the causes of the measurement errors. The meaning of the 7 calibration parameters can be summarised as follows:

- a_0 — Fixed offset term, corresponding to a shift of the measurement origin
- a_1 — Linear term in distance, corresponding to a scale factor, perhaps due to a shift in modulation frequency
- a_2, a_3 — Amplitudes of sinusoidal functions at 4 times the modulation frequency. This can occur due to systematic shifts in sensor readings (see section 3.3)

- a_4, a_5 — Amplitudes of sinusoidal functions at 8 times the modulation frequency. This can occur due to components at the third or fifth harmonic present in the impure modulation signal (see section 3.2)
- a_6 — Linear factor of the radial distance. This could be caused by systematic optical effects at large viewing angles, or due to an offset of the camera origin (see section 2.4)

The explanation of these terms is the great benefit of this model over high-order polynomials, or b-splines [3], where the values of the parameters do not help with the understanding of the causes.

The values of the 7 parameters vary according to the modulation frequency used. The offset a_0 is between -47 and -7 mm, the scale a_1 is between 1% and 2%, the amplitudes a_2 to a_5 are all on the order of 10 mm, and the radial factor a_6 is around 7.

After application of this calibration, the rms errors were reduced to around 11 mm for the first set of data. Using a second, independent set of data, the previously calculated parameters were applied, giving rms residuals between 11.4 mm and 12.5 mm. This is a strong validation that the calibration was successful and that the calibration parameters remain valid for future measurements.

It is certainly beneficial that the calibration in this study was performed using white circular targets. Other studies have used checkerboard patterns [6] or arrangements of rectangles [2]. Circular targets avoid edge effects as measurements are always taken from the middle of a uniform section of the image.

In addition, the response of the camera to continuous use was found to be consistent with a temperature-dependent shift in the modulation frequency. A few minutes of continuous operation caused all distance measurements to increase by between 1 and 2%, and the wraparound distance to be reduced by the same factor. This suggests that the oscillator is sensitive to temperature and generates a higher frequency signal when warmed by prolonged use.

References

1. T. Kahlmann: Range Imaging Metrology: Investigation, Calibration and Development, ETH Zürich (2007)
2. D. Lichti: Self-Calibration of a 3D Range Camera, ISPRS Congress Beijing (2008)
3. M. Lindner, A. Kolb and T. Ringbeck: New Insights into the Calibration of TOF Sensors, IEEE Conf. on Computer Vision and Pattern Recognition (2008)
4. H. Rapp: Experimental and Theoretical Investigation of Correlating TOF-Camera Systems, Diploma thesis, University of Heidelberg (2007)
5. T. Ringbeck: A 3D Time of Flight Camera for Object Detection, Conference on Optical 3D Measurement Techniques (2007)
6. I. Schiller, C. Beder and R. Koch: Calibration of a PMD-Camera Using a Planar Calibration Pattern Together with a Multi-Camera Setup, ISPRS Congress Beijing (2008)